ADVANCES IN ATMOSPHERIC SCIENCES, VOL. 41, JANUARY 2024, 97–114

• **Original Paper** •

Case Studies of the Microphysical and Kinematic Structure of Summer Mesoscale Precipitation Clouds over the Eastern Tibetan Plateau

Shuo JIA[1,2], Jiefan YANG[*1], and Hengchi LEI[1,2]

[1]*Key Laboratory of Cloud-Precipitation Physics and Severe Storms*, *Institute of Atmospheric Physics*, *Chinese Academy of Sciences*, *Beijing* 100029, *China*

[2]*University of Chinese Academy of Sciences*, *Beijing* 100049, *China*

(Received 18 October 2022; revised 30 March 2023; accepted 12 April 2023)

ABSTRACT

Three cases of microphysical characteristics and kinematic structures in the negative temperature region of summer mesoscale cloud systems over the eastern Tibetan Plateau (TP) were investigated using X-band dual-polarization radar. The time–height series of radar physical variables and mesoscale horizontal divergence $\bar{\delta}$ derived by quasi-vertical profiles (QVPs) indicated that the dendritic growth layer (DGL, −20°C to −10°C) was ubiquitous, with large-value zones of K_{DP} (specific differential phase), Z_{DR} (differential reflectivity), or both, and corresponded to various dynamic fields (ascent or descent). Ascents in the DGL of cloud systems with vigorous vertical development were coincident with large-value zones of Z_{DR}, signifying ice crystals with a large axis ratio, but with no obvious large values of K_{DP}, which differs from previous findings. It is speculated that ascent in the DGL promoted ice crystals to undergo further growth before sinking. If there was descent in the DGL, a high echo top corresponded to large values of K_{DP}, denoting a large number concentration of ice crystals; but with the echo top descending, small values of K_{DP} formed. This is similar to previous results and reveals that a high echo top is conducive to the generation of ice crystals. When ice particles fall to low levels (−10°C to 0°C), they grow through riming, aggregation, or deposition, and may not be related to the kinematic structure. It is important to note that this study was only based on a limited number of cases and that further research is therefore needed.

Key words: Tibetan Plateau, polarimetric variables, microphysics, dendritic growth layer, kinematic structure, aggregation, riming

Citation: Jia, S., J. F. Yang, and H. C. Lei, 2024: Case studies of the microphysical and kinematic structure of summer mesoscale precipitation clouds over the eastern Tibetan Plateau. *Adv. Atmos. Sci.*, **41**(1), 97–114, https://doi.org/10.1007/s00376-023-2303-7.

Article Highlights:

- The DGL was ubiquitous, with large-value zones of K_{DP}, Z_{DR}, or both, and corresponded to ascent or descent.
- In clouds with vigorous vertical development, ascent in the DGL stimulated ice crystals to undergo further growth before sinking.
- When there was descent in the DGL, the accompanying high echo top was conducive to the generation of ice crystals.
- At a low level, ice crystals formed in the DGL grew via riming, aggregation and deposition, perhaps unrelated to the kinematic structure.

1. Introduction

As the highest and largest plateau in the world, the topography of the Tibetan Plateau (TP) has an important impact on atmospheric circulation and water vapor transportation (Yeh and Chang, 1974; Xu et al., 2014). Its dynamic and thermal effects determine the monsoon climate characteristics of East Asia (Wu and Zhang, 1998; Li et al., 2001; Xu et al., 2010). With the largest total radiation in summer and extending to the middle troposphere, the TP also has a significant impact on the cloud precipitation processes of local and downstream regions (Xu et al., 2019).

In recent decades, a series of studies on clouds over the TP have been performed, most of which focused on convective clouds and precipitation in summer, and the results suggest some unique characteristics. For instance, convective clouds over the plateau are usually characterized by their cold cloud base, low water vapor content, few ice nuclei, thin cloud thickness, and high ice-crystallization temperature

* Corresponding author: Jiefan YANG
Email: yjf@mail.iap.ac.cn

(Wang et al., 2002; Fujinami et al., 2005; Dai et al., 2011; Yue et al., 2018). Recently, using the data obtained during the Third Tibetan Plateau Atmospheric Scientific Experiment (Zhao et al., 2018), Chang et al. (2019) found that plateau convective clouds with limited vertical velocity and few cloud condensation nuclei tend to produce wide cloud droplet spectra. Analysis based on multi-source observation data from satellites and ground-based vertically pointing radars revealed that deep convective clouds are mainly ice clouds dominated by mixed-phase and glaciation processes (Wang and Guo, 2018). With abundant supercooled water at −20°C to 0°C, snow and graupel particles have the characteristics of high content and deep vertical distribution, and graupel grows mainly via aggregation and riming (Tang et al., 2018). Furthermore, research found that deep or shallow convective clouds correspond to different vertical motion characteristics (Ruan et al., 2018; Pang et al., 2019), and the strength of ascent affects microphysical processes in the clouds (Zhang et al., 2019).

Interesting Z_{DR} (differential reflectivity) or K_{DP} (specific differential phase) signatures, observed in the −20°C to −10°C layer of US winter storms and European stratiform clouds, are thought to be indications of dendritic crystals (DCs) and plate-like ice crystals, and are known as the dendritic growth layer (DGL) (Ryzhkov et al., 1998; Bechini et al., 2013; Griffin et al., 2014; Schrom et al., 2015). Kennedy and Rutledge (2011) reported an elevated layer of local K_{DP} maxima near the −15°C isotherm, and the passage of this region was associated with an increase in surface precipitation (Trömel et al., 2019). Later, Andrić et al. (2013) found that enhancement in Z_{DR} and K_{DP} regions was coincident with a large vertical gradient of radar reflectivity (Z_H). Regions of ascent were consistently associated with polarimetric signatures, implying planar crystal growth when near −15°C (Bailey and Hallett, 2009; Kumjian and Lombardo, 2017). Several repetitive signatures for the correlation between Z_{DR} or K_{DP} in the DGL and the cloud tops have been observed (Griffin et al., 2018). Williams et al. (2015) identified two kinds of features of enhanced Z_{DR} and large or small Z_H in winter and summer stratiform systems coincident with water-saturated or insufficient amounts of supercooled water environments.

To sum up, the above studies mainly focused on the DGL in winter storms and its characteristics influenced by ascent and its effect on precipitation. Considering that glaciation processes are predominant in summer clouds and precipitation, which may be affected by vertical motion over the TP, we aim to investigate whether there are also DGLs in summer mesoscale precipitation clouds over the TP. If there are, corresponding microphysical characteristics and possible effects of vertical motion will be analyzed, and the similarities and differences compared with previous studies will be discussed. This is of great significance for improving the parameterization schemes of numerical models and the forecasting skill for precipitation in this region.

The remainder of the paper is structured as follows: We first introduce the field campaign and datasets in section 2. The methods of radar data preprocessing and reconstruction are presented in section 3. In section 4, time–height series of physical variables are applied to analyze the macroscopic and microphysical features, and kinematic structure, during different precipitation processes, with particular attention paid to investigating the microphysical characteristics in the negative temperature region, especially the DGL and the influence of dynamic fields on it. Finally, a summary, conclusions and some further discussion are provided in section 5.

2. Field experiment

2.1. *Instruments and data*

The field campaign was organized by the China Meteorological Administration in associated with the Institute of Atmospheric Physics, Chinese Academy of Sciences. Figure 1a shows the location of the measurement site. One of the main goals of this field campaign was to improve understanding of the macrophysical and microphysical characteristics and vertical structure of summer precipitation clouds over the eastern TP. For this purpose, multiple instruments, including an X-band dual-polarization Doppler radar, K-band micro-rain radar, Ka-band cloud radar, microwave radiometer, and particle size velocity (Parsivel) disdrometer, were deployed in Zeku County, Qinghai Province, between August and September from 2019 to 2021.

An X-band dual-polarization Doppler radar (referred to as ZKXR) is located in Zeku County (35.038°N, 101.47°E) (Fig. 1a, red five-pointed star). Its main specifications are summarized in Table 1, among which its observation range of 75 km means it can only cover part of the mesoscale cloud system we are concerned about. The observations of ZKXR are set in a volume coverage pattern (VCP) consisting of 12 layers with elevation angles from 1.8° to 19.5°, which takes 6–7 min per volume scan. This provides high spatial and temporal resolution base data, including the Z_H, radial velocity (V_R), Z_{DR}, differential propagation phase shift (Φ_{DP}), and correlation coefficient (ρ_{hv}), which have been extensively applied to the analysis of microphysical processes in clouds and precipitation (Schneebeli et al., 2013; Picca et al., 2014; Jensen et al., 2016), hydrometeor classification (Snyder et al., 2010; Dolan et al., 2013), and estimation of quantities such as ice water content, particle diameter, and number concentration (Ryzhkov et al., 2018; Ryzhkov and Zrnić, 2019).

A vertically pointing K-band MRR is located at the same station. It works with an operating frequency of 24 GHz and a beamwidth of 2° (Table 1) and produces spectral Doppler density data, with a range resolution of 200 m and a temporal resolution of 1 min. The vertical profile of the raindrop size distribution (DSD) is provided by the MRR, and parameters such as the rain intensity, echo intensity, and liquid water content can be retrieved from this DSD (Wang et al., 2017).

To match the analysis, vertical profiles of temperature over the observation area will be required, but there are no

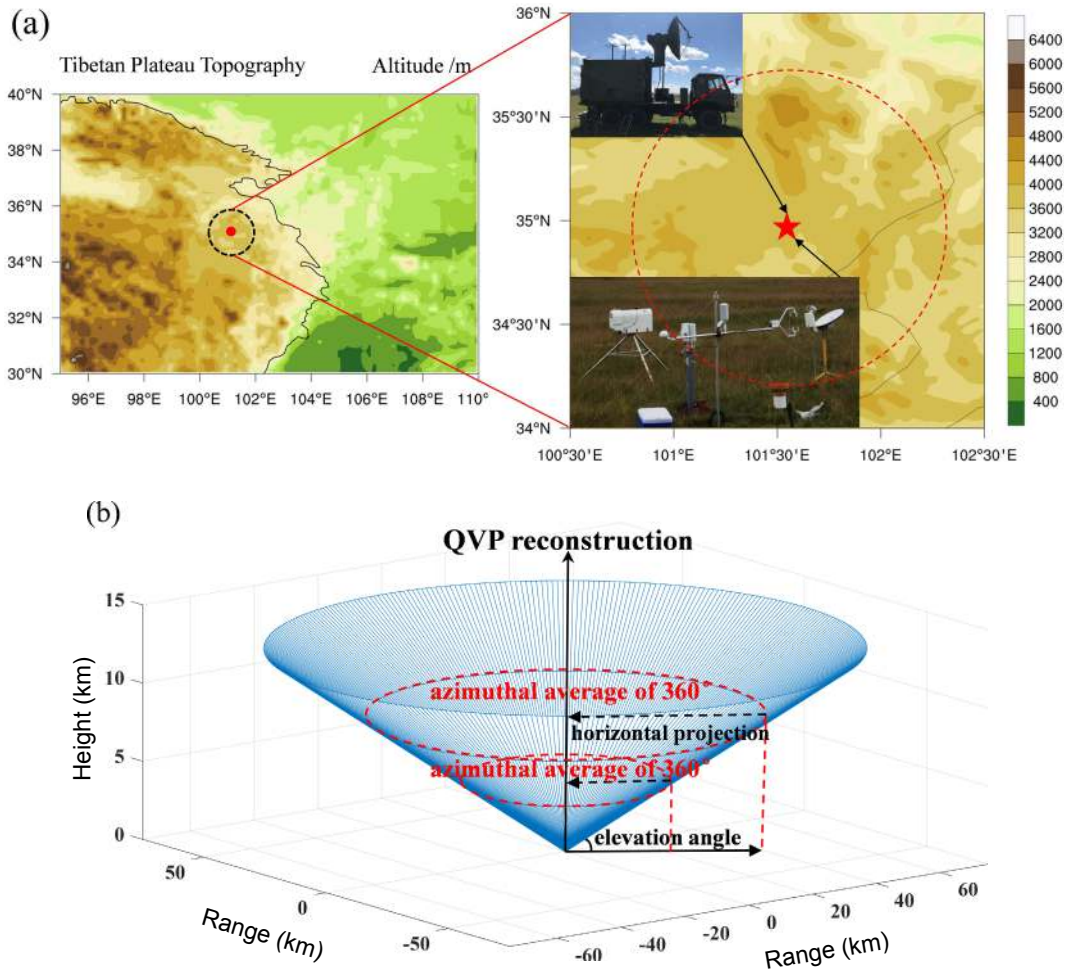

Fig. 1. (a) Topography in the experimental area and instruments (red star denotes the radar station). (b) Quasi-vertical profile (QVP) reconstruction based on plane position indicator (PPI) scanning data.

Table 1. System specifications of the ZKXR and micro rain radar (MRR).

	ZKXR	MRR
Operating frequency	9.4 GHz	24.23 GHz
Peak power	75 kW	50 mW
Antenna diameter	2.4 m	0.6m
Beam width	0.97°	2°
Transmission mode	Simultaneous horizontal and vertical transmission	Frequency-modulated continuous wave
Range resolution	75 m	200 m
Range gate	1000	31
Sampling time	6–7 min	1 min

conventional radiosonde stations within 100 km of the radar station. Therefore, the thermodynamic and dynamic fields from the fifth major global reanalysis produced by ECMWF (ERA5) data, with a 0.25° × 0.25° resolution (Hersbach et al., 2018), are employed for supplementary information, which are available from hourly reanalysis climate datasets made available by ECMWF.

2.2. *Synoptic situation*

In this paper, we mainly focus on the mesoscale cloud precipitation systems in summer over the eastern TP, which are relatively uniform horizontally with less unstable energy. Referring to existing studies (Chang, 2019; Zhang et al., 2021), the main synoptic situation controlling the cloud precipitation systems in the rainy season include a plateau shortwave trough pattern, east-high and west-low pattern, and zonal circulation pattern. We selected three cases from the limited observation period belonging to these kinds of synoptic situations—namely, 17–18 September, 7–8 August, and 12 August 2021 (Table 2).

Table 2. Cases analyzed in this study and their corresponding synoptic situation.

Date	Synoptic situation
17–18 September 2021	Plateau shortwave trough
7–8 August 2021	East-high and west-low pattern
12 August 2021	Zonal circulation pattern

At 1400 and 2000 LST [except when noted, time is referred to as local standard time (LST) in the following sections, LST=UTC+8] 17 September, a 500-hPa West Asia trough located in the Balkesh Lake area moved eastward, the bottom of which slid down to form a shortwave trough over the plateau (Figs. 2a and b). Blocked by a subtropical anticyclone, the shortwave trough moved at a slower speed, leading warm and humid southwest air carrying a large amount of water vapor. Therefore, the cloud system developed deeply and lasted longer than one day. At 2000 LST 7 August, a 500-hPa subtropical anticyclone extended westward and northward (Fig. 2c), bringing warm and humid air, accompanied by upper cold air, leading to unstable atmospheric stratification. This process consisted of convective and stratiform clouds. At 0800 LST 12 August, a strong low pressure system was observed in Siberia and eastward on the 500-hPa isobaric surface (Fig. 2d). The experimental area was in the flat westerly flow at the bottom of the low pressure, in which a shortwave trough moved eastward, with the southerly wind transporting water vapor at the low level continuously. Therefore, low-level and medium-level clouds formed with stable atmospheric stratification in summer. In general, it can be summarized that the duration of the 17–18 September case was the longest, with a good water vapor condition in the upper part; the unstable energy of the 7–8 August case was relatively large; and the unstable energy of the 12 August case was relatively small, with a good water vapor condition in the low level.

After quality control and attenuation correction of radar volume-scanning data (see section 3.1), an overview of the evolution of precipitation during the three cases is presented based on PPI at a 6.4° elevation angle. From 1800 to 2200 LST 17 September, radar echoes developed rapidly (Z_H > 35 dBZ) (Fig. 3a) and maintained in a strong stage. After 2200 LST, radar echoes from west (Fig. 3b), northwest and southwest of the radar station indicated a stratus configuration and the reflectivity gradually weakened (< 30 dBZ). Radar echoes gradually developed once again from 0500 LST (Fig. 3c) and strengthened locally over the radar station after 1100 LST (Fig. 3d). From PPIs during the 7–8 August precipitation case (Figs. 3e–h), the cloud system successively experienced a wide range of strong echoes (from 2000 to 2200 LST, Z_H > 40 dBZ), scattered weak echoes (from 2300 to 0100 LST), and relatively strong echoes moving in (from 0200 to 0400 LST, Z_H > 40 dBZ). During the 12 August precipitation process (Figs. 3i–l), the cloud system was in peri-

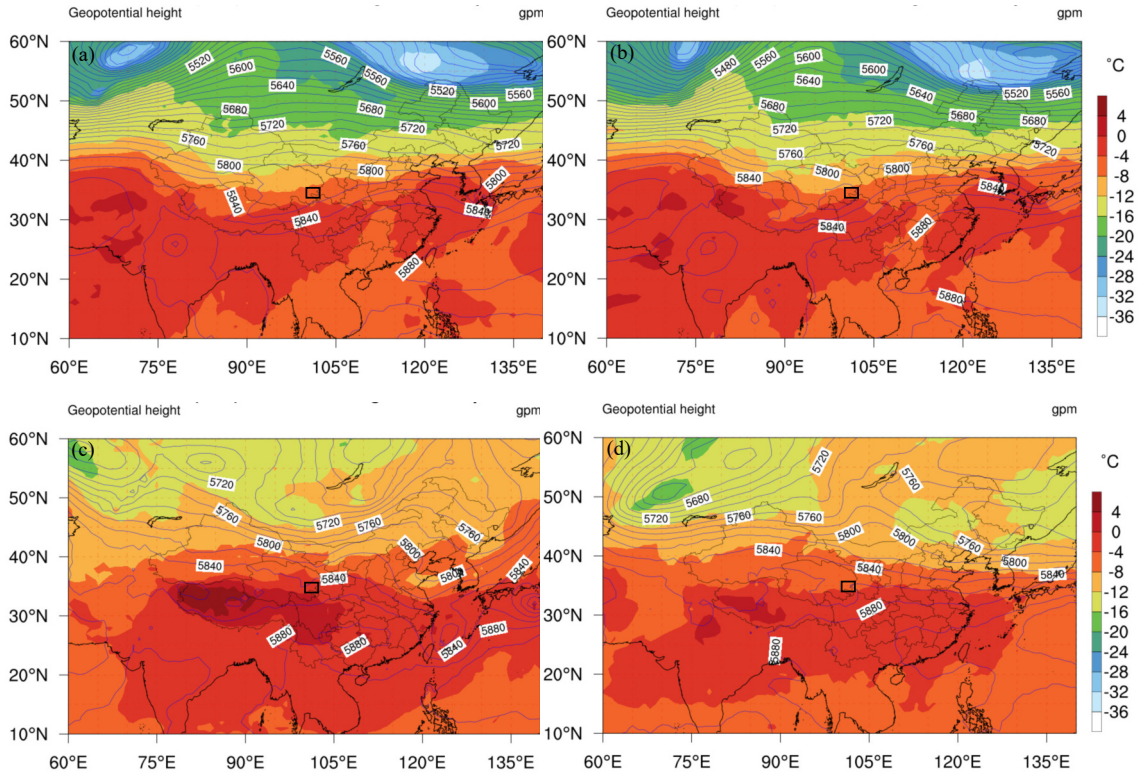

Fig. 2. Synoptic situation at 500 hPa at (a) 1400 LST and (b) 2000 LST 17 September 2021; (c) 2000 LST 7 August 2021; and (d) 0800 LST 12 August 2021 (contours: geopotential height; color shading: temperature; black rectangle: area of interest).

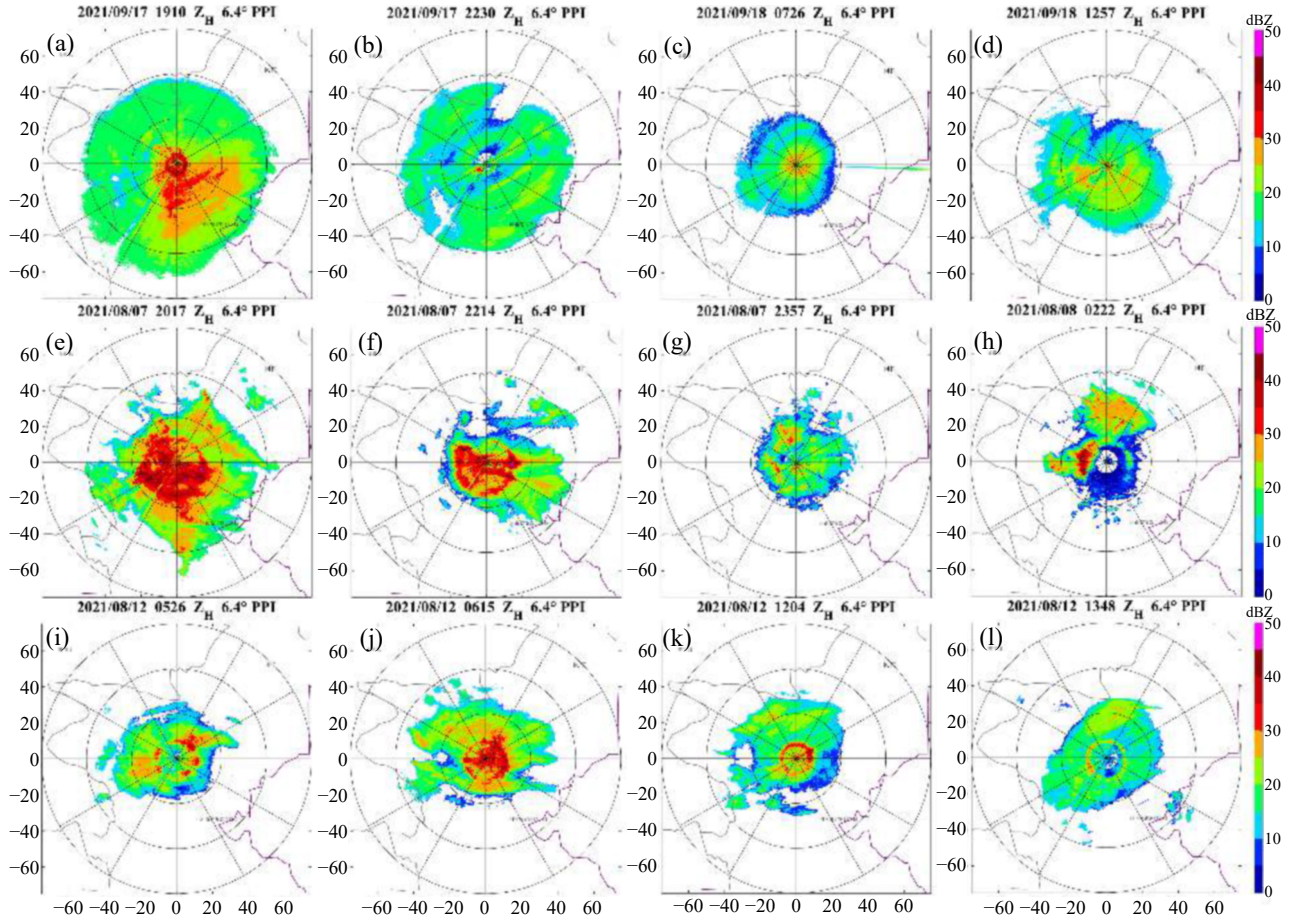

Fig. 3. The 6.4° PPI of ZKXR at (a) 1910 and (b) 2230 LST 17 September 2021; (c) 0726 and (d) 1257 LST 18 September 2021; (e) 2017, (f) 2214 and (g) 2357 LST 7 August 2021; (h) 0222 LST 8 August 2021; and (i) 0526, (j) 0615, (k) 1204 and (l) 1348 LST 12 August 2021.

odic development, with the echo intensity first increasing ($Z_H > 40$ dBZ) and then decreasing.

Combined with surface hourly precipitation data, the precipitation duration of the 17–18 September case was the longest, and the regional average accumulated precipitation was the largest (12.58 mm), but the regional average hourly precipitation was the smallest (0.52 mm). In the 7–8 August case, the precipitation duration was shortest and the regional average hourly precipitation was largest (0.89 mm). The regional average hourly precipitation of the 12 August case was 0.68 mm. All cases had liquid-phase precipitation on the ground, except the 17–18 September case, which occurred with precipitation phase transformation (liquid–ice–liquid). As a result, the maximum Z_H during the first case was smaller than in the other two cases.

3. Methods

3.1. *Data preprocessing*

First, the ZKXR raw data used in this paper are preprocessed. Data with Z_H smaller than 15 dBZ, ρ_{hv} smaller than 0.8, and an absolute value of V_R smaller than 1.0 m s^{-1} are regarded as non-meteorological echoes and excluded from the analysis (Ryzhkov and Zrnić, 1998). To eliminate noise effects, a moving average filter is applied to different variables with different range gates. Then, the Z_{DR} bias is corrected using the PPI at low elevation angles in drizzle regions (Bringi et al., 2001; Park et al., 2005). Additionally, ρ_{hv} is corrected with the signal-to-noise ratio (SNR) by adopting the method described in Shusse et al. (2009). Lastly, raw data with SNRs lower than 20 dB are excluded while saving the ZKXR VCP data.

Next, the value of K_{DP} is calculated from Φ_{DP} by piecewise linear regression using least-squares fitting over a range that varies with the Z_H level following the conventional algorithm (Wang and Chandrasekar, 2010). Once K_{DP} has been determined, the Z_H and Z_{DR} below the melting layer are corrected for rainfall attenuation with K_{DP} following Jameson (1992), with the height of 0°C isotherms estimated from ERA5 data.

Furthermore, the temperature of each layer from the hourly ERA5 data is interpolated to obtain the isotherm heights from −20°C to 0°C for assisting in analyzing the

microphysical and kinematic vertical structure of clouds in the negative temperature area.

3.2. *QVP reconstruction of physical variables*

To obtain high-resolution vertical profiles of radar variables to analyze the fine microphysical structure of clouds, the quasi-vertical profile (QVP) method (Ryzhkov et al., 2016) is used. Moreover, a method of estimating horizontal divergence $\bar{\delta}$ based on QVPs of V_R (Kumjian and Lombardo, 2017) is also applied to infer the kinematic structure.

3.2.1. *Polarimetric variables*

In the method, PPI data at every radial gate are averaged along the full azimuth and projected horizontally to a vertical axis within a conical volume to obtain the QVP (Fig. 1b). Theoretically, when the cloud system is horizontally uniform within the conical volume, the high-resolution profiles obtained can represent the vertical structure of cloud well compared to conventional methods such as GridRad (Homeyer and Bowman, 2017). Although such averaging may smooth out the small-scale horizontal structure, the noise in the polarimetric variables can also be significantly reduced (Ryzhkov et al., 2016).

The effective vertical resolution of QVPs can be approximately estimated as the larger of the two terms

$$\Delta h_1 = \Delta r \sin\alpha\,, \tag{1}$$

and

$$\Delta h_2 = h\Delta\theta\cot\alpha\,, \tag{2}$$

where Δr is the radial range gate (75 m), α is the antenna elevation angle, h is the height above the ground and, $\Delta\theta$ is the beam width (0.97°). The vertical resolution is approximately 96 m at $h = 2$ km and 191 m at $h = 4$ km, which is significantly better than other interpolation methods. However, due to the effect of beam broadening, the vertical resolution deteriorates with increasing height (Ryzhkov et al., 2016).

Usually, PPI data at high elevation angles are selected to reconstruct QVPs to reduce adverse factors such as beam broadening, horizontal inhomogeneity of the cloud system, and hydrometeor falling speed. Considering that the focus in this paper is a mesoscale cloud system in a limited area, the QVPs of Z_H, Z_{DR} and K_{DP} are reconstructed by using PPI data at an elevation angle of 19.5°.

3.2.2. *Horizontal divergence*

The QVP of V_R can be reconstructed by the above method, which suggests net convergence (divergence) at a given height corresponding to a radial gate (Doviak and Zrnić, 2006):

$$\langle V_R\rangle = \frac{1}{2\pi}\int_0^{2\pi} V_R(\phi)\,\mathrm{d}\phi\,, \tag{3}$$

where $\langle V_R\rangle$ signifies the azimuthally averaged V_R over 360°, obtained by the QVP method.

The relation between V_R and $\bar{\delta}$ can be obtained assuming that there is a horizontal linear wind field in the conical scanning area (Kumjian and Lombardo, 2017):

$$\langle V_R\rangle = \frac{1}{2}a_0 = \frac{1}{2}\bar{\delta} r\cos\theta_e + w\sin\theta_e. \tag{4}$$

Here, θ_e is the elevation angle with respect to the radar, and r is the radial range from the radar. In addition, $\bar{\delta} = \partial u/\partial x + \partial v/\partial y$ represents the horizontal divergence, in which the overbar indicates regional averaging. Because the averaging of vertical atmospheric motion over a relatively wide range can be ignored, the vertical velocity w is thus mainly determined by the hydrometeor falling speed.

However, because the terminal velocities of raindrops are too large to be ignored, the $\bar{\delta}$ field below the 0°C isotherm is not considered in the estimation. The falling speed of ice-phase hydrometeors at a 9.9° elevation angle is empirically assumed to be approximately 1 m s^{-1}. Therefore, the second term on the right-hand side can be neglected relative to the divergence term in Eq. (4), and QVPs of V_R can be used to estimate mesoscale horizontal divergence/convergence ($\bar{\delta}$) into the conical scan region. Negative/positive values usually represent net convergence/divergence.

Consequently, as is shown in Fig. 4, ascent/descent is implied by the vertical convergence–divergence dipole. Convergence in the lower layer and divergence in the upper layer correspond to ascent (Fig. 4a), while divergence in the lower layer and convergence in the upper layer indicate descent (Fig. 4b). Therefore, based on the vertical profile of $\bar{\delta}$, we can infer the characteristics of the kinematic structure in the conical region.

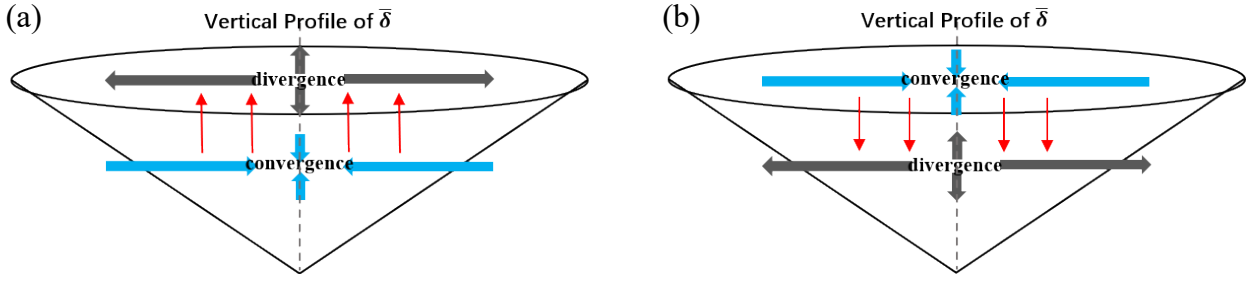

Fig. 4. The (a) ascent and (b) descent implied by the estimated convergence–divergence dipoles at each layer in the conical scanning volume.

4. Results

4.1. *The 17–18 September 2021 case*

4.1.1. *Time–height series of Z_H and $\bar{\delta}$ reconstructed using the QVP method*

To verify whether the vertical profiles of ZKXR physical variables reconstructed by QVP show the characteristics of the radar echo appropriately, the reconstructed time–height series of Z_H is compared with the vertical pointing observations of the nearby MRR. Meanwhile, the ERA5 divergence data at grid points in every layer that are closest to ZKXR are chosen to compare with the $\bar{\delta}$ estimated by the V_R-based QVP.

The time–height series of Z_H provided by continuous QVPs (Fig. 5a) is consistent with the fluctuation shown by

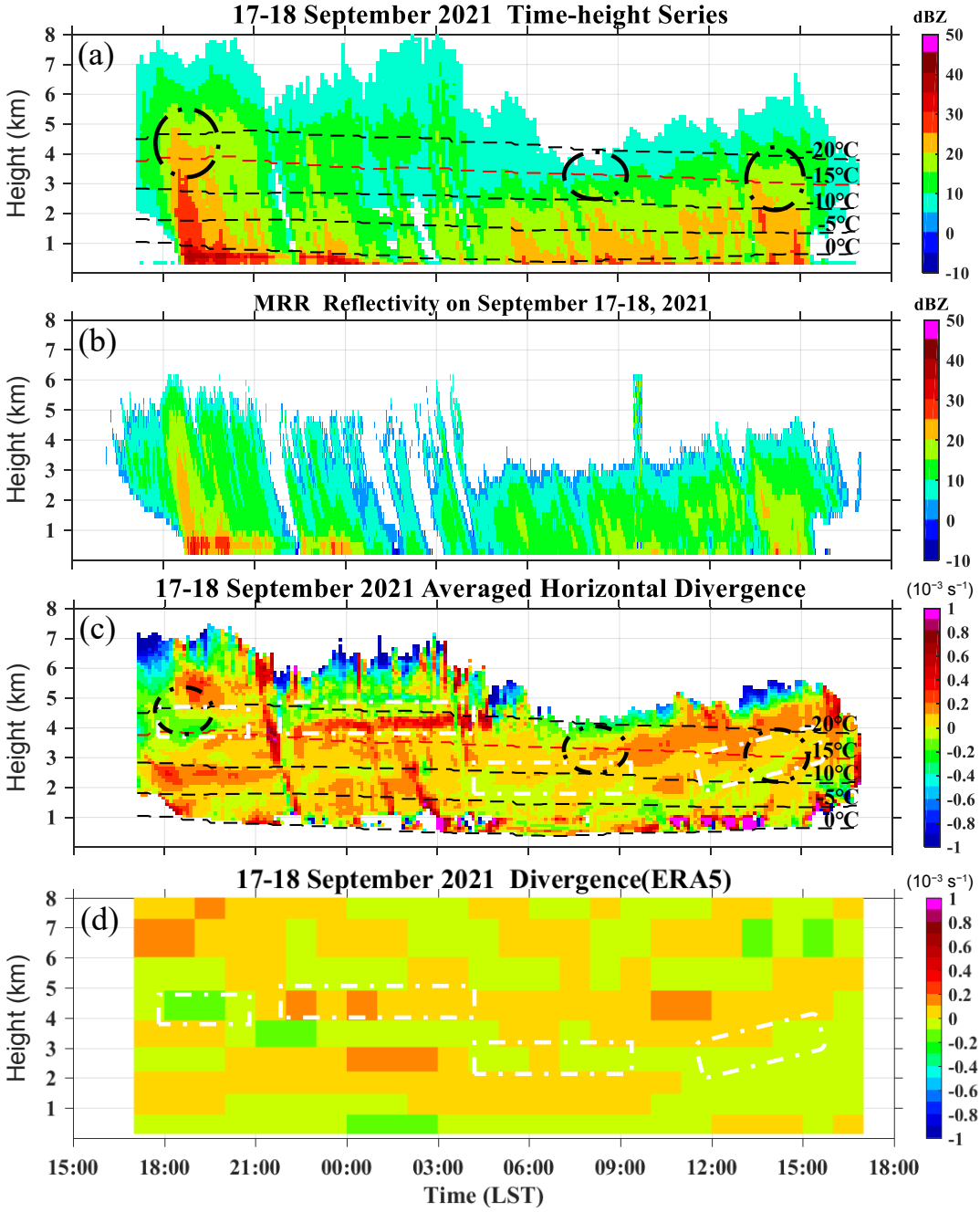

Fig. 5. Comparison of the Z_H time–height series between (a) that reconstructed by the QVP method and (b) that of the MRR, and of the $\bar{\delta}$ time–height series between (c) that estimated by V_R QVPs and (d) that of the ERA5 reanalysis data, during the 17–18 September 2021 case. From low to high, the black lines are the 0°C, −5°C, −10°C and −20°C isotherms, and the red line is the −15°C isotherm. The black dashed circles denote the DGL indicated by the characteristics of polarimetric variables, and the white dashed boxes represent the ascent/descent layers indicated by the convergence–divergence dipoles.

the MRR (Fig. 5b) in terms of the cloud top and precipitation core. It should be noted that the echo top height displayed by the MRR is slightly lower than that reconstructed by the QVP method based on ZKXR data, which can be attributed to the shorter wavelength of the MRR and the attenuation in echo intensity caused by near-surface precipitation. As a result, the overall echo intensity of the MRR is also weaker than that of the ZKXR.

The time–height series of $\bar{\delta}$ (Fig. 5c) established based on QVPs of V_R shows that its vertical distribution varied with fluctuation in the echo top and intensity. Prominent convergence appeared at approximately 4 km in the rapid development phase of clouds (from 1800 to 2100 LST; white dashed boxes in Fig. 5c), with divergences above and below. A similar convergence–divergence dipole was also indicated by the ERA5 data (white dashed boxes in Fig. 5d), but the vertical range was slightly different because of their different temporal and spatial resolutions. From 2200 LST, the radar echo stratified and gradually weakened. There was a strong divergence in the vicinity of 4 km, with weak convergence above. The ERA5 data showed some discrepancies in the conversion of the convergence or divergence layer over time. After 0400 LST 18 September, the convergence dropped below 3 km and divergence appeared above it, with the echo in the lower layer strengthening. The vertical ranges of the convergence and divergence layers from the ERA5 data were different to some extent. The convergence rose above 3 km after 1200 LST, and divergence was observed above it, and the ERA5 data suggested the same distribution as the former. In general, compared with the ERA5 divergence data, the time–height series of $\bar{\delta}$ indicated a more detailed vertical distribution of horizontal divergence, which is coincident with the evolutionary characteristics of echo reflectivity.

4.1.2. *Microphysical processes and kinematic structure*

Figure 6 shows the time–height series of polarimetric variables (Z_{DR}, K_{DP}) with ERA5 hourly temperature data overlaid. Before 1930 LST, large-value zones of Z_{DR} and K_{DP} in the negative temperature zone were simultaneously observed near the −20°C to −10°C layer (Fig. 6, black dashed circle) with a weak radar echo (Fig. 5a, black dashed circle), consistent with the DGL characteristics demonstrated in previous studies (Ryzhkov et al., 1998; Bechini et al., 2013; Schrom et al., 2015). Furthermore, the time–height series of $\bar{\delta}$ indicated that ascent implied by the convergence–divergence dipole appeared above −15°C (Fig. 5c, black dashed circle). Similar large-value features also presented from 0730 to 1000 LST, with the echo top height and strong echo decreasing significantly (Fig. 5a). The characteristics of the large-value zone were slightly different, with a large-value zone of K_{DP} presented in the −15°C to −10°C layer (a lower height) and Z_H and Z_{DR} increasing rapidly, coincident with descent implied by the convergence–divergence dipole above the −15°C isotherm but ascent below it. From 1330 to 1500 LST, with the echo top height and strong echo increasing again, a large-value zone of K_{DP} rose above the −15°C isotherm, while enhancements in Z_H and Z_{DR} presented in the −20°C to −10°C layer. Different from the previous

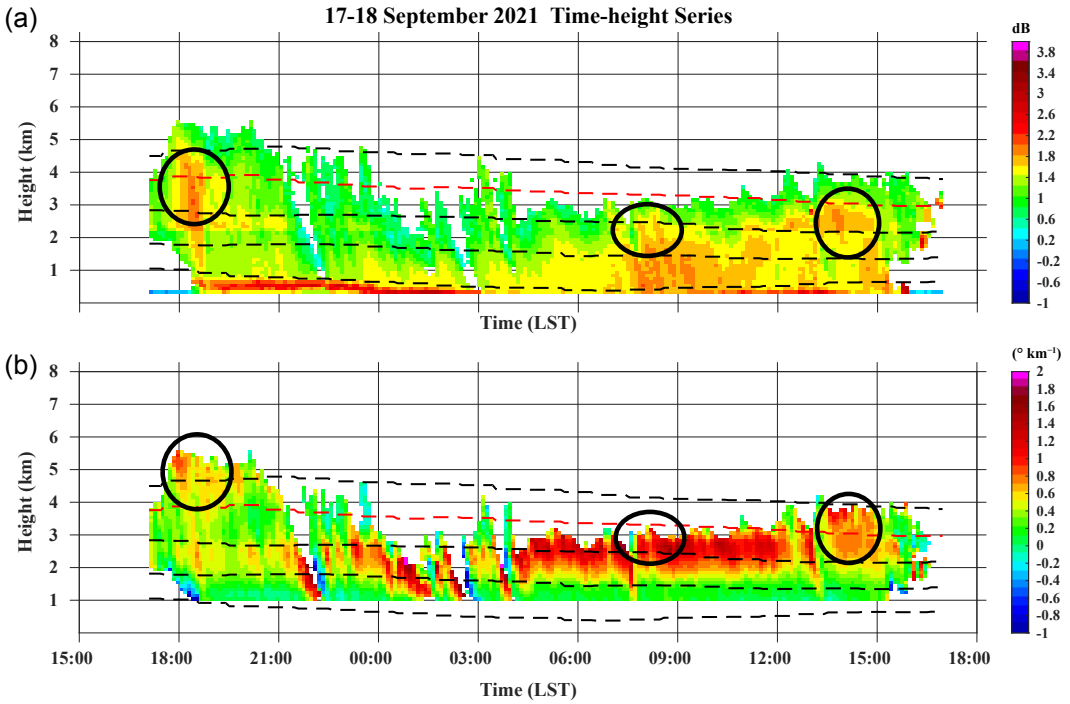

Fig. 6. Time–height series of (a) Z_{DR} and (b) K_{DP} reconstructed by the QVP method during 17–18 September 2021. From low to high, the black lines are the 0°C, −5°C, −10°C and −20°C isotherms, and the red line is the −15°C isotherm. The black circles denote the DGL indicated by the characteristics of polarimetric variables.

two periods, only weak ascent straddled the −15°C isotherm.

In summary, it can be concluded that a DGL appeared in the −20°C to −10°C layer during the periods of 1800–1930 LST 17 September and 0730–1000 and 1330–1500 LST 18 September, which we refer to as "typical periods". However, with the decrease in echo top height, the DGL was coincident with descent, and its characteristics of polarimetric variables were different. An analysis of the occurrence frequency and variations of the radar physical variables with height during each typical period will be made in the following, focusing on investigating the microphysical characteristics in the negative temperature region and the influence of kinematic structure on it.

Based on the reconstructed and established time–height series of radar physical variables, the frequencies of Z_H, Z_{DR}, K_{DP} and $\bar{\delta}$ occurrence with height during the typical periods (1800–1930, 0730–1000 and 1330–1500 LST) are presented in Fig. 7 with vertical profiles of medians overlapped (solid red line).

During the period between 1800 and 1930 LST, K_{DP} above −20°C gradually decreased from the maximum (median of 0.5° km^{-1}) (Fig. 7c), indicating that pristine ice crystals with a certain number concentration were formed (Kennedy and Rutledge, 2011). Z_{DR} increased rapidly in the −20°C to −15°C layer (Fig. 7b), with a median of up to 1.5 dB, corresponding to gradually increasing Z_H with a median of approximately 20 dBZ (Fig. 7a). These are associated with vigorous dendritic growth and the onset of aggregation between −20°C and −15°C isotherms (Williams et al., 2015), coincident with ascent implied by the $\bar{\delta}$ field (Fig. 7d). A slight enhancement in Z_H and a reduction in Z_{DR} and K_{DP} in the −15°C to −7°C layer are commonly attributed to aggregation of ice-phase particles, as particles decrease in effective density and their axis ratio becomes close to unity (Bechini et al., 2013; Schneebeli et al., 2013). As the height continued to drop to the 0°C isotherm, Z_{DR} and K_{DP} decreased significantly (close to 0° km^{-1}), while Z_H increased significantly. It is speculated that ice-phase particles rime to generate graupel. The partial melting of graupel

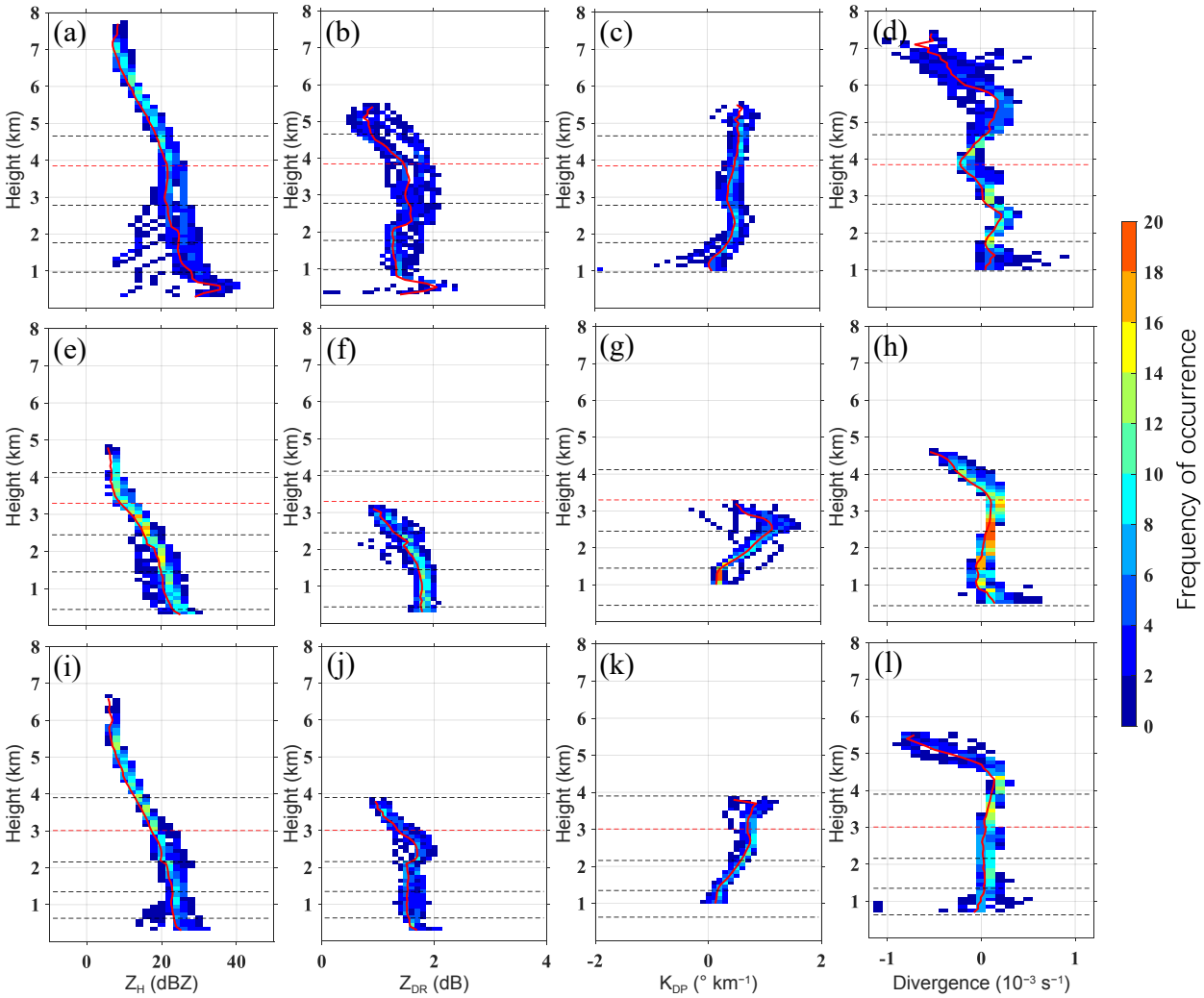

Fig. 7. Frequency of occurrence (color shading) and median (solid red line) of physical variables in the period (a–d) 1800–1930, (e–h) 0730–0900 and (i–l) 1330–1500 LST 17–18 September 2021. Horizontal dashed lines denote the −20°C, −15°C, −10°C, −5°C and 0°C isotherms, from top to bottom.

near the 0°C isotherm leads to a significant increase in Z_H and Z_{DR}, which decrease with graupel melting into the complete liquid phase.

The height of isotherms decreased during the period 0730–0900 LST. Descent implied by the convergence–divergence dipole was presented above the −15°C isotherm (Fig. 7h), with a weak echo and lack of polarimetric measurements. K_{DP} reached its maximum (median of 1.1° km^{-1}) in the −15°C to −10°C layer (Fig. 7g), which is thought to signify a large number concentration of ice crystals, implying highly efficient aggregation (Moisseev et al., 2015; Schrom et al., 2015). Noticeable increases in Z_H and Z_{DR} (medians of 15 dBZ and 1.4 dB, respectively) were presented as well (Figs. 7e and f), with weak ascent below, indicating the generation of DCs. The significant reduction of K_{DP} and the moderate enhancement in Z_H and Z_{DR} in the −10°C to 0°C layer could therefore be ascribed to the aggregation and deposition of ice-phase particles.

From 1330 to 1500 LST, there was descent implied by the $\bar{\delta}$ field (Fig. 7l) above −20°C with polarimetric variables not measured as well. The thickness of isotherms between 0°C and −20°C decreased, suggesting cold advection consistent with the wind field from the ERA5 data. With weak ascent near the −15°C isotherm, the polarimetric characteristics in the −20°C to −10°C layer were similar to those of the first typical period, with the maximum K_{DP} (Fig. 7k, median of 0.7° km^{-1}) higher than that of Z_{DR} (Fig. 7j, median 1.6° km^{-1}), indicating the generation of DCs, but the heights of large-value zones were generally lower than those of the 1800–1930 LST period. In the lower layer of −10°C to 0°C, Z_H (Fig. 7i) and Z_{DR} were almost unchanged, and K_{DP} decreased rapidly, which may be related to weak aggregation and deposition of ice-phase particles, like in the second typical period.

In summary, with different vertical development of echoes, there are some similarities and differences in the kinematic structures and microphysical characteristics of the DGLs (−20°C to −10°C) among the three typical periods. The characteristics of polarimetric variables in the DGL during the three typical periods are similar in that the large-value zones of K_{DP} appear above the ascent, and then the large-value zones of Z_{DR} appear below the ascent. The ascent implied by the $\bar{\delta}$ field in the first and third typical periods appeared higher (above −20°C, near −15°C) than that in the second period (−10°C). The differences are as follows: Ascent and similar features of polarimetric variables were presented in the DGLs during the first and third periods, with K_{DP} gradually decreasing from the maximum, Z_{DR} gradually increasing to the maximum, and Z_H gradually increasing. This is consistent with the DGL characteristics suggested by Schrom et al. (2015), indicating generation of DCs with a big axis ratio. However, during the second typical period, there was descent in the DGL, and the maximum K_{DP} was significantly large, while the large-value zone of Z_{DR} was not obvious, indicating a large number concentration of DCs generating, but with an axis ratio close to 1. Therefore, it is concluded that when the DGL at −20°C to −10°C corresponds to ascent, the corresponding Z_{DR} and Z_H are large; but with descent, the corresponding Z_{DR} and Z_H are small, and K_{DP} is large.

Previous studies have shown large ice supersaturation over the TP. Thus, many ice crystals could be formed in the −20°C to −10°C layer via deposition. A small air density over the plateau results in ice crystals with an axis ratio close to 1 (corresponding to a small Z_{DR}) tending to fall, and ice crystals could undergo further growth with ascent in the DGL (the first and third periods) before sinking (Sulia and Harrington, 2011), leading to a large Z_{DR} (big axis ratio) and Z_H. However, without ascent presented in the DGL during the second period, a large number concentration of ice crystals is conducive to forming with a smaller Z_{DR}, a larger K_{DP}, and a smaller Z_H.

The DCs grow through aggregation and riming in the first typical period but through aggregation and deposition in the other two typical periods when they fall into the −10°C to 0°C layer. Combined with the vertical distribution of the $\bar{\delta}$ field, it is considered that microphysical processes in the −10°C to 0°C layer have nothing to do with the kinematic structure. Only a large-value layer of Z_H and Z_{DR} presented near the 0°C isotherm during the first typical period, indicating a transformation in the precipitation phase, and there was ice-phase precipitation near the surface during the last two typical periods, due to the isotherms descending obviously.

4.2. *The 7–8 August 2021 case*

4.2.1. *Time–height series of $\bar{\delta}$ reconstructed using the QVP method*

The same as with the first case, the ERA5 divergence data at grid points closest to ZKXR are chosen to compare with the $\bar{\delta}$ estimated based on QVPs of V_R. The time–height series of $\bar{\delta}$ shows that divergence or convergence alternately appeared between 4 km and 5 km before 2200 LST, and divergence occurred mainly below it. The vertical distribution of divergence or convergence revealed by the ERA5 data was different from the former, as well as its change over time. After 0200 LST, descent implied by the convergence–divergence dipole was observed near 3 km, and the vertical structure of the divergence field shown by the ERA5 data was consistent with that. In conclusion, when the vertical development of radar echoes is strong with a high echo top, the ERA5 data cannot show the vertical structure of the divergence field accurately compared with the $\bar{\delta}$ estimated by QVPs of V_R. The characteristics of the two are consistent in the weak vertical development stage.

4.2.2. *Microphysical processes and kinematic structure*

Figure 8 shows the time–height series of radar variables (Z_H, Z_{DR}, K_{DP}) and $\bar{\delta}$ with ERA5 hourly temperature data overlaid. Combined with PPIs of ZKXR, two strong echoes passed through the radar station from 2000 to 2130 LST sequentially, with echo tops close to 8 km (Fig. 8a). From 2020 LST, there was descent implied by the convergence–

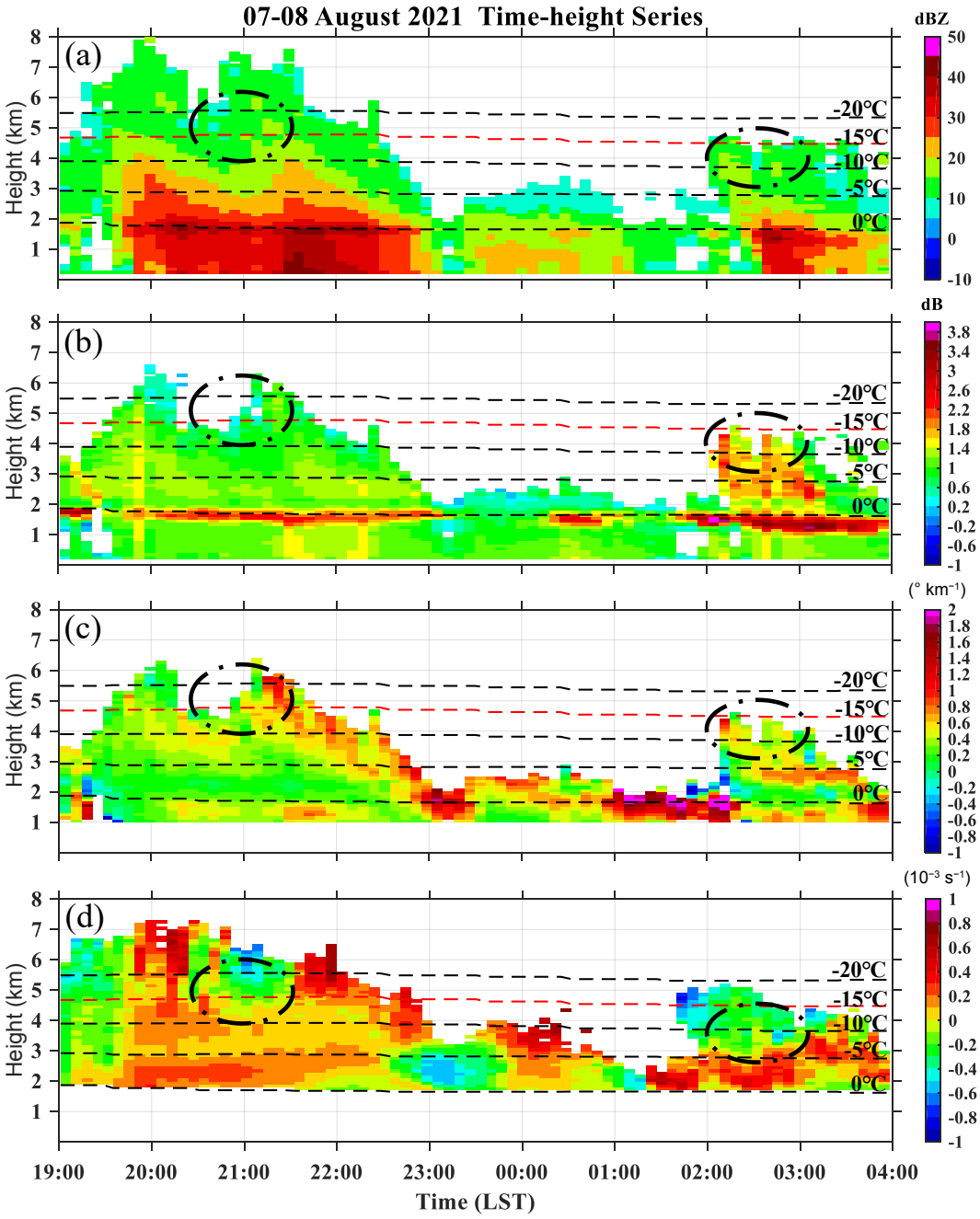

Fig. 8. Time–height series of the (a) Z_H, (b) Z_{DR}, (c) K_{DP}, and (d) $\bar{\delta}$ reconstructed by the QVP method for the 7–8 August 2021 case. From low to high, the black lines are the 0°C, −5°C, −10°C and −20°C isotherms, and the red line is the −15°C isotherm. The black dashed circles denote the DGL indicated by the characteristics of polarimetric variables.

divergence dipole near the −15°C isotherm (Fig. 8d), with the echo top height and strong echo descending and then increasing again. A large-value zone of K_{DP} (0.6°–1.0° km^{-1}) in the negative temperature region, with small Z_H (< 20 dBZ) appearing in the −20°C to −10°C layer (Figs. 8c and 8a). From 0210 LST, the radar echo developed again, descent appeared near the −10°C isotherm, along with a large-value zone of K_{DP} (0.5°–0.8° km^{-1}) and large Z_{DR} (1.6–2.2 dB) (Fig. 8b) above it, while Z_H was still smaller than 20 dBZ.

It can be concluded that the typical periods with DGL characteristics in the −20°C to −10°C layer were 2020–2130 LST 7 August and 0210–0315 LST 8 August. Compared with the process on 17 and 18 September, the DGLs were coincident with descent, with small Z_H (< 20 dBZ), and a significant increase in echo intensity was concentrated in the −5°C to 0°C layer. An analysis of the occurrence frequency and variations of radar variables (Z_H, Z_{DR}, K_{DP}) and $\bar{\delta}$ with height during each typical period will be made in the following, focusing on investigating the microphysical characteristics in the negative temperature region and the influence of

the kinematic structure on it.

The frequencies of Z_H, Z_{DR}, K_{DP} and $\bar{\delta}$ occurrence with height during the typical periods (2020–2130 and 0210–0315 LST) are presented in Fig. 9 with vertical profiles of medians overlaid (solid red line).

During the period from 2020 to 2130 LST, the maximum K_{DP} (median of 1° km^{-1}) appeared near the −20°C isotherm (Fig. 9c), coincident with a small value of Z_{DR} (Fig. 9b, median of 0.9 dB), suggesting the generation of pristine ice crystals (including DCs). Then, K_{DP} gradually decreased and Z_{DR} remained unchanged in the −20°C to −10°C layer, with a small enhancement in Z_H (Fig. 9a, median of 16 dBZ), corresponding to the descent implied by the $\bar{\delta}$ field near the −15°C isotherm (Fig. 9d) and indicating deposition and aggregation of ice crystals (Andrić et al., 2013; Schneebeli et al., 2013). The scattered frequency distributions of Z_{DR} and K_{DP} implied that the size and density of generated ice-phase particles varied greatly. In the −10°C to 0°C layer, K_{DP} decreased (median close to 0° km^{-1}) and Z_{DR} gradually increased (median of 1.2 dB), coincident with Z_H increasing significantly (median of 25 dBZ). It is speculated that ice-phase particles grew through riming with supercooled water.

From 0210 to 0315 LST, the height of isotherms descended. The maximum K_{DP} (median of 0.4° km^{-1}) (Fig. 9g) at −15°C to −10°C was smaller than that in the first period, coincident with a slight enhancement in Z_{DR} (Fig. 9f, median of 1.5 dB) and Z_H (Fig. 9e, median of 13 dBZ), coincident with descent near the −10°C isotherm (Fig. 9h). Combined with the relatively scattered frequency distribution of Z_{DR} (0.8–2.0 dB), it is thought that various types of ice crystals (including DCs) were formed, with a small number concentration and large deviation in the axis ratio. Z_{DR} and K_{DP} gradually increased to their maximums and then decreased in the −10°C to 0°C layer, with Z_H first invariant and then increasing significantly (median close to 20 dBZ), possibly indicating that ice-phase particles underwent deposition and riming, accompanied by secondary ice crystal production (Griffin et al., 2018).

Large-value layers of Z_H and Z_{DR} [namely, the melting layer (ML)] all presented near the 0°C isotherm (Figs. 9b and f) in the two typical periods. Through comparison between the height of the ML and 0°C isotherm, it is speculated that the height of the 0°C isotherm from the ERA5 data was lower than the actual value in the first typical period. Graupel becomes flat and the dielectric constant increases after melting, resulting in the increasing axis ratio and reflectivity, so Z_H and Z_{DR} increase considerably in the ML. In addition, it takes a longer path to complete melting for graupel than aggregation (Giangrande et al., 2016), so the thickness of the ML is larger compared with the 17–18 September process.

In general, there are large-value zones of K_{DP} in the DGLs during the two typical periods of the 7–8 August process, coincident with descent implied by the convergence–divergence dipole. When the echo top reached a high height between 2020 and 2130 LST, large K_{DP} denoting a large number concentration of DCs generated appeared near the −20°C isotherm. However, with the echo top descending during the period from 0210 to 0315 LST, small K_{DP} and large

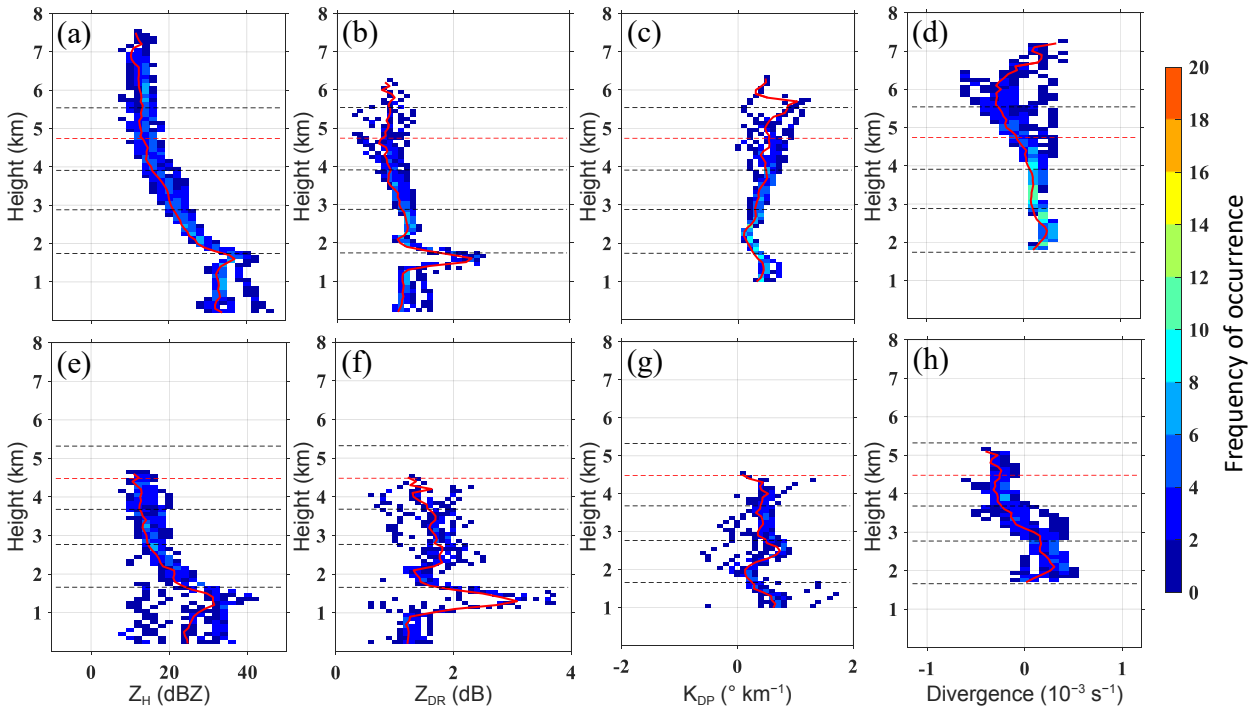

Fig. 9. Frequency of occurrence (color shading) and median (solid red line) of physical variables in the periods (a–d) 2020–2130 LST and (e–h) 0210–0315 LST 7–8 August 2021. Horizontal dashed lines denote the −20°C, −15°C, −10°C, −5°C and 0°C isotherms, from top to bottom.

Z_{DR} denoted that various types of ice crystals (including DCs) were formed at −15°C to −10°C, with a large axis ratio and small number concentration. This reveals that if there is descent in the DGL, a high echo top is conducive to the generation of DCs, as indicated by large K_{DP}, which is similar to the results demonstrated by Griffin et al. (2018) for the ice-phase microphysical processes of snowfall. Ice crystals formed in the DGLs went through aggregation and deposition, then grew mainly by riming in the falling process under the DGL, which may have nothing to do with the kinematic structure implied by the $\bar{\delta}$ field. Comparing the growth rates of Z_H from echo tops to 0°C isotherms, it is found that the growth rate of Z_H in the first typical period is larger than that in the second period. So, it is speculated that DCs with a large number concentration are conducive to rime with supercooled water, which leads to the development and strengthening of a low-level echo in the negative temperature region.

4.3. *The 12 August 2021 case*

4.3.1. *Time–height series of $\bar{\delta}$ reconstructed using the QVP method*

The time–height series of $\bar{\delta}$ showed that convergence or divergence alternately occurred between 3 km and 4 km before 0900 LST, and divergence was mainly below it. From 0900 to 1200 LST, with radar echo development, ascent implied by $\bar{\delta}$ appeared below 3 km, and divergence was located above it. After 1200 LST, the echo top was slightly reduced, and there was descent between 3 km and 4 km. After 1500 LST, prominent convergence appeared at approximately 3 km. By comparing the divergence field from the ERA5 data of grid points closest to ZKXR with the former, there are some differences in the shift and vertical distribution of convergence or divergence before 1200 LST. After that, with the echo top lowering and cloud structure tending to be stable, the vertical distribution of the divergence field was consistent with the former, but with different large values. In terms of the reason, analysis indicates that when the mesoscale cloud system moved and developed quickly, the ERA5 divergence data, with their limited vertical and temporal resolution and incomplete consideration of underlying surface factors, had poor representation.

4.3.2. *Microphysical processes and kinematic structure*

Figure 10 shows the QVPs of radar variables (Z_H, Z_{DR}, K_{DP}) and estimated $\bar{\delta}$ in a time versus height format on 12 August 2021 with ERA5 hourly temperature data overlaid. The time–height series of Z_H (Fig. 10a) indicates that the echo top maintained at approximately 5 km (−20°C) as a whole (Fig. 10a), while the strong echo (>20 dBZ) top height and strong echo center fluctuated. Polarimetric signatures and the dynamic field of the cloud system are then analyzed.

Descent implied by the convergence–divergence dipole occurred above the −15°C or −10°C isotherm before 0900 LST (Fig. 10d). From 0500 to 0600 LST, K_{DP} showed maximums (0.6°–1.0° km^{-1}) in the negative temperature region near the −15°C isotherm (Fig. 10c), corresponding to a weak echo (Fig. 10a, Z_H < 15 dB), which is consistent with the characteristics of the DGL investigated in the 7–8 August process. With further echo development, large-value zones of K_{DP} (0.8°–1.2° km^{-1}) and Z_{DR} (1.6–2.4 dB) appeared in the −20°C to −10°C layer between 0800 and 0900 (Figs. 10c and 10b), coincident with descent near the −10°C isotherm and Z_H < 20 dBZ. After 1200 LST, the echo top descended, and large-value zones of K_{DP} (0.6°–0.8° km^{-1}) appeared at −15°C to −10°C, coincident with descent in this layer.

In general, it can be concluded that characteristics of DGLs appeared in the −20°C to −10°C layer during the periods of 0500–0600, 0800–0900 and 1220–1420 LST 12 August, which we refer to as "typical periods". There was descent in the DGLs, which were all located near the echo top in this process. An analysis focusing on investigating the microphysical characteristics in the negative temperature region and the influence of the kinematic structure on it will be made in the following.

Based on the reconstructed and established time–height series of radar physical variables, the frequencies of Z_H, Z_{DR}, K_{DP} and $\bar{\delta}$ occurrence with height during the typical periods (0500–0600, 0800–0900 and 1220–1420 LST) are presented in Fig. 11, with vertical profiles of medians overlapped (solid red line).

During the period from 0500 to 0600 LST, there are maximums of K_{DP} (median of 0.8° km^{-1}) and Z_{DR} (median of 1.4 dB) in the negative temperature region near the −15°C isotherm (Figs. 11c and 11b), with small echo reflectivity (Fig. 11a, median of 10 dBZ), coincident with descent below it (Fig. 11d), which indicates vigorous dendritic growth in the DGL. In the −15°C to −10°C layer, with Z_H gradually increasing, almost invariant Z_{DR}, and K_{DP} decreasing (median of 0.3° km^{-1}), it is speculated that ice crystals grow by aggregation (mainly) and deposition. The polarimetric signatures in the −10°C to 0°C layer were similar to those in the period of 0210–0315 LST 8 August, which suggests that ice-phase particles deposited to accumulate rime, accompanied by secondary ice crystal production.

Between 0800 and 0900 LST, K_{DP} (median of 0.9° km^{-1}) and Z_{DR} (median of 2.6 dB) decreased from the maximums of the negative temperature zone in the −20°C to −15°C layer (Fig. 11g, f) with a relatively scattered frequency distribution, while Z_H increased slightly (Fig. 11e), coincident with descent near the −10°C isotherm (Fig. 11h). It is inferred that there are many types of ice crystals (including DCs) generated, and they grow by aggregation (mainly) and deposition, indicated by invariant Z_{DR}, prominently decreasing K_{DP}, and slightly increasing Z_H in the −15°C to −5°C layer. Dropping to the −5°C to 0°C layer, K_{DP} decreased (close to 0° km^{-1}) and values of Z_{DR} were more concentrated and unchanged, coincident with gradually increasing Z_H, indicating that ice-phase particles rime with supercooled water.

From 1220 to 1420 LST, descent implied by the

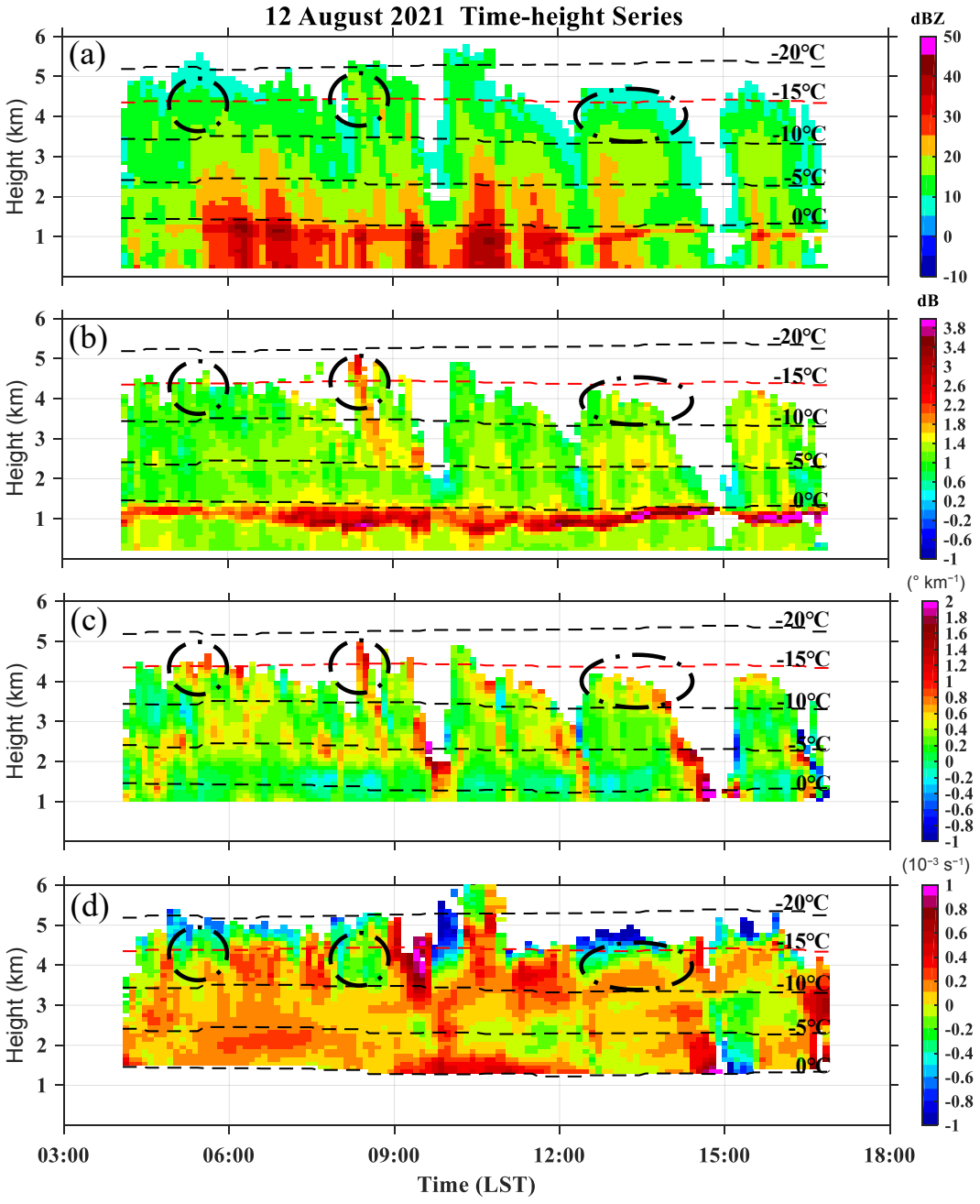

Fig. 10. Time–height series of the (a) Z_H, (b) Z_{DR}, (c) K_{DP} and (d) δ reconstructed by the QVP method on 12 August 2021. From low to high, the black lines are the 0°C, −5°C, −10°C and 20°C isotherms, and the red line is the −15°C isotherm. The black dashed circles denote the DGL indicated by the characteristics of polarimetric variables.

convergence–divergence dipole presented in the −15°C to −10°C layer (Fig. 11l). K_{DP} gradually decreased from the maximum of the negative temperature region (Fig. 11k, median of 0.5° km^{-1}) in this layer, corresponding to a median of Z_{DR} close to 1.2 dB (Fig. 11j) and a large enhancement in Z_H (Fig. 11i, median of 17 dBZ), which suggests that DCs formed and aggregated but with a small number concentration. In the −10°C to −5°C layer, Z_H increased slightly, Z_{DR} first increased and then decreased, and K_{DP} decreased gradually, suggesting that ice-phase particles grew by deposition and riming. The scattered frequency distribution of Z_{DR} and K_{DP} implies that the size and density of ice-phase particles varied greatly.

Furthermore, there were large-value layers of Z_H and Z_{DR} below the 0°C isotherms during the three typical periods, resulting from the generated graupel melting into a liquid state gradually, with a higher dielectric constant and flatter particle shape compared to ice-phase graupel. After melting into water droplets completely, Z_H and Z_{DR} decreased from large values owing to the volume reduction and close to

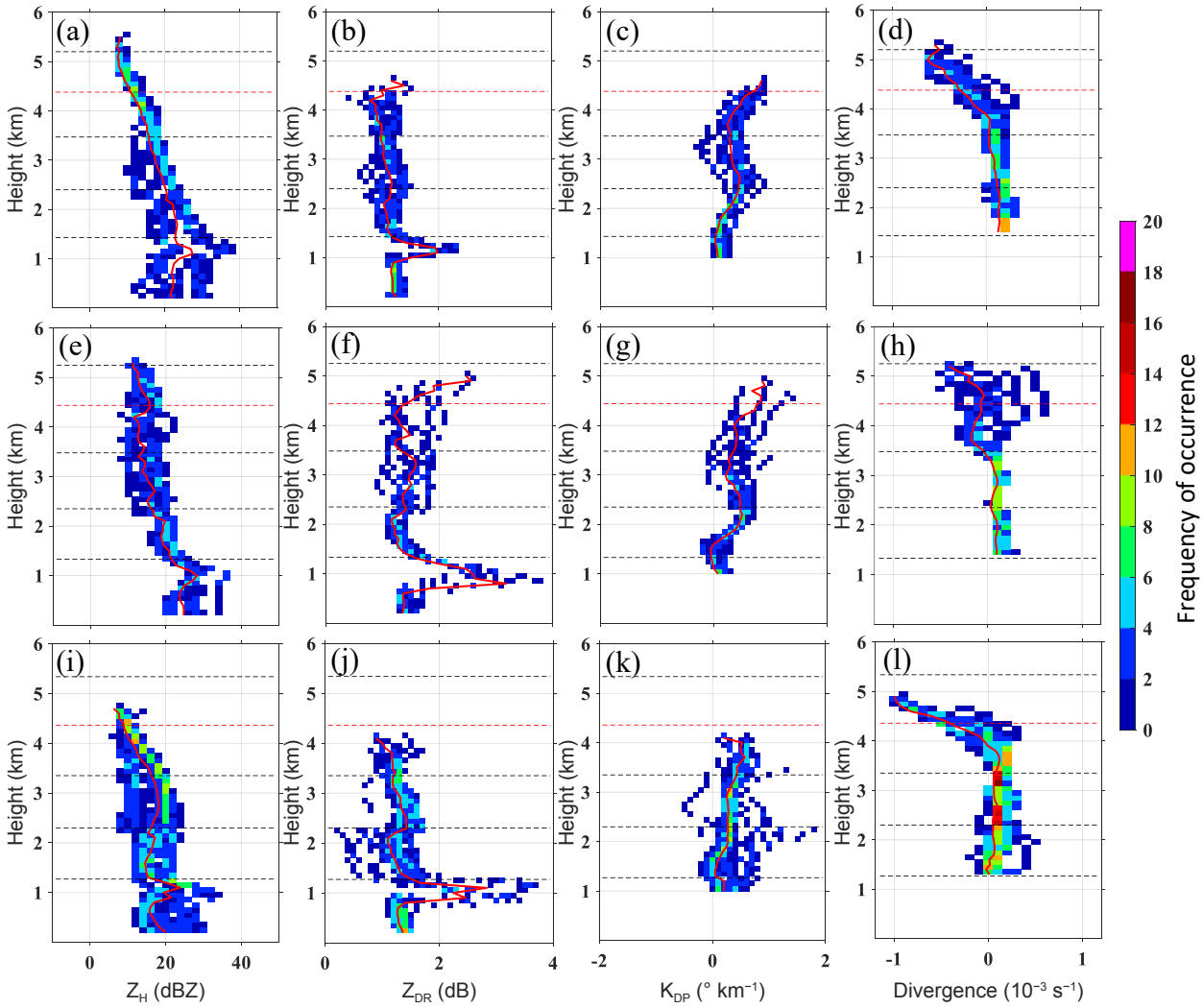

Fig. 11. Frequency of occurrence (color shading) and median (solid red line) of physical variables during (a–d) 0500–0600, (e–h) 0800–0900 and (i–l) 1220–1420 LST 12 August 2021. Horizontal dashed lines denote the −20°C, −15°C, −10°C, −5°C and 0°C isotherms, from top to bottom.

round shape.

In summary, the DCLs with large-value zones of K_{DP} located near the echo top were all coincident with descent in the three typical periods of the 12 August process. With the echo top height varying, large-value zones of K_{DP} (0.8°–0.9° km^{-1}) were located above the descent implied by convergence –divergence dipoles in the first two periods, while that of the third period was located below descent with a median of 0.5° km^{-1}. As K_{DP} is proportional to the number concentration (e.g., Ryzhkov et al., 1998), it is speculated that, with descent in the DGL, a high echo top indicates relatively vigorous radar echo development (low temperature, high supersaturation with respect to ice), which results in a large number concentration of ice crystals (including DCs) generating (Chu et al., 2018), indicated by large values of K_{DP}. The positive correlation between the K_{DP} values in the DGLs and echo top heights in the typical periods was similar to that of the 7–8 August process, corresponding to a weak echo (Z_H < 20 dBZ). As with the microphysical processes, generated ice crystals (including DCs) first usually go through aggregation, and then grow by deposition and riming with the production of secondary ice crystals in the falling process under the DGL, which is thought to have nothing to do with the kinematic structure implied by the $\bar{\delta}$ field. We compared the Z_H growth rates from echo tops to 0°C isotherms, and could infer similar results that the formation of DCs with a large number concentration is more conducive to riming and echo enhancement at the lower level.

5. Summary and discussion

This study provides insight into three cases of microphysical processes and corresponding kinematic structures in the negative temperature region of summer mesoscale cloud systems over the eastern TP, based on transportable X-band dual-polarization radar VCP data. The latest QVP reconstruction method and estimation algorithm were applied to establish time–height series of radar physical variables and

mesoscale horizontal divergence $\bar{\delta}$.

The reconstructed time–height series of Z_H was compared with vertical-pointing observations of a nearby MRR, allowing us to conclude that the two were consistent in terms of the cloud echo top and precipitation core. Meanwhile, ERA5 divergence data at grid points in each layer were used to compare with the $\bar{\delta}$ estimated by V_R-based QVP. The results showed that the estimated $\bar{\delta}$ accurately captured the vertical distribution of the divergence field, and the two were consistent in the weak vertical development stage of the cloud system, which we attributed to the ERA5 data not fully considering the influence of the underlying surface over the TP, and the limited vertical and temporal resolutions.

Next, the time–height series of radar physical variables (Z_H, Z_{DR}, K_{DP}) and $\bar{\delta}$, with ERA5 hourly temperature data overlaid, were used to investigate the characteristics of polarimetric variables and kinematic structures in the mesoscale cloud systems. We focused on the microphysical characteristics in the DGL of selected typical periods with DGL features and assessed the possible mechanism of dynamic field influence on microphysical processes. The vertical distribution of $\bar{\delta}$ was applied to innovatively analyze the dynamic field in the DGL.

DGL signatures like those found in winter storms over plains also exist in summer mesoscale precipitation clouds over the eastern TP, such as large-value zones of either K_{DP} or Z_{DR}, or both, in the −20°C to −10°C layer. Three cases of mesoscale cloud systems affected by different kinds of typical synoptic situations (including a plateau shortwave trough pattern, east-high and west-low pattern, and zonal circulation pattern) were analyzed and compared with each other. There were apparent discrepancies of polarimetric characteristics and microphysical processes in the DGLs with various dynamic fields. The main conclusions are as follows:

In the case of 17–18 September 2021, the cloud system developed vigorously and the echo top fluctuated. Various features of polarimetric variables with ascent or descent were implied by the convergence–divergence dipole in the DGLs, so the influence of the dynamic field on microphysical processes in the DGL was analyzed. Large-value zones of Z_{DR} representing a big axis ratio of DCs presented when there was ascent in the DGLs, but with small K_{DP} values denoting a limited number concentration of DCs. While there was descent in the DGL, a large-value zone of K_{DP} representing a large number concentration of DCs presented, but large values of Z_{DR} were not obvious. These results are different from previous research (Kumjian et al., 2014; Moisseev et al., 2015). It is speculated to be related to atmospheric background conditions, and ice crystals could undergo further growth with ascent in the DGL before sinking (Sulia and Harrington, 2011). Therefore, during the typical periods, large-value zones of K_{DP} usually appeared above the ascent, and large-value zones of Z_{DR} appeared below the ascent.

In the two August 2021 cases, the vertical development of the cloud systems was slightly weaker overall. There were large-value zones of K_{DP} with no obvious large values of Z_{DR} in the DGLs during the typical periods, all coincident with descent implied by the convergence–divergence dipoles. Obvious differences in vertical development of cloud systems are thought to result in different maximums of K_{DP}. When the echo top reached a high height, large K_{DP}, denoting a large number concentration of DCs, generated and appeared in the DGLs; however, with the echo top descending, small K_{DP} formed. This is similar to the results reported by Griffin et al. (2018) regarding the ice-phase microphysical processes of snowfall, and reveals that when there is descent in the DGL, a high echo top is conducive to the generation of ice crystals, with large-value zones of K_{DP} above the descent.

When falling to a low level (−10°C to 0°C), ice crystals formed in the DGLs went through aggregation, deposition, and riming during the different typical periods, which may have nothing to do with the kinematic structure. Ice crystals with a large axis ratio are more likely to grow by aggregation. The formation of ice crystals with large number concentrations is conducive to riming and echo enhancement at the lower level. During the typical periods with liquid-phase precipitation near the surface, there were large-value layers of Z_H and Z_{DR} presented near the 0°C isotherm, i.e., the ML, indicating a transformation of particle phase.

The QVP method is suitable for the reconstruction of cloud systems with uniform horizontal distributions. Certain assumptions should be met when estimating $\bar{\delta}$ by QVPs of V_R; that is, the wind field in the conical scanning area changes linearly. Due to a lack of reliable observation data, the effects of water vapor conditions on microphysical processes were not considered in this paper. Special observations, such as those made by aircraft in-situ instruments, need to be added and applied for comparison and verification in future studies. Also, it is important to note that this study only investigated a limited number of cases. Further research is needed to establish general features of the cloud structure over the eastern TP based on statistical analysis.

Acknowledgements. This study was jointly funded by the Northwest Regional Weather Modification Capacity Building Project of the China Meteorological Administration (Grant No. ZQC-R18209) and the National Natural Science Foundation of China (Grant Nos. 41875172 and 42075192). We greatly appreciate the strong support of the project team and Weather Modification Office of Qinghai Province in the organization and implementation of the field experiment. Furthermore, we thank Dr. Liang FENG and Dr. Hong WANG for their guidance and suggestions on the data preprocessing.

REFERENCES

Andrić, J., M. R. Kumjian, D. S. Zrnić, J. M. Straka, and V. M. Melnikov, 2013: Polarimetric signatures above the melting layer in winter storms: An observational and modeling study. *J. Appl. Meteorol. Climatol.*, **52**(3), 682–700, https://doi.org/10.1175/JAMC-D-12-028.1.

Bailey, M. P., and J. Hallett, 2009: A comprehensive habit diagram for atmospheric ice crystals: Confirmation from the laboratory, AIRS II, and other field studies. *J. Atmos. Sci.*, **66**, 2888–2899, https://doi.org/10.1175/2009JAS2883.1.

Bechini, R., L. Baldini, and V. Chandrasekar, 2013: Polarimetric radar observations in the ice region of precipitating clouds at C-band and X-band radar frequencies. *J. Appl. Meteorol. Climatol.*, **52**(5), 1147–1169, https://doi.org/10.1175/JAMC-D-12-055.1.

Bringi, V. N., T. D. Keenan, and V. Chandrasekar, 2001: Correcting C-band radar reflectivity and differential reflectivity data for rain attenuation: A self-consistent method with constraints. *IEEE Trans. Geosci. Remote Sens.*, **39**(9), 1906–1915, https://doi.org/10.1109/36.951081.

Chang, Y., 2019: The summer cloud microphysical characteristics and precipitation formation processes derived from aircraft observation in the Naqu region over the Tibetan Plateau. PhD dissertation, Chinese Academy of Meteorological Sciences, 101 pp. (in Chinese)

Chang, Y., X. L. Guo, J. Tang, and G. X. Lu, 2019: Aircraft measurement campaign on summer cloud microphysical properties over the Tibetan Plateau. *Scientific Reports*, **9**, 4912, https://doi.org/10.1038/s41598-019-41514-5.

Chu, X., L. L. Xue, B. Geerts, and B. Kosović, 2018: The impact of boundary layer turbulence on snow growth and precipitation: Idealized large eddy simulations. *Atmospheric Research*, **204**, 54–66, https://doi.org/10.1016/j.atmosres.2018.01.015.

Dai, J., X. Yu, G. H. Liu, X. H. Xu, Z. G. Yue, W. Sun, and F. Z. Yang, 2011: Satellite retrieval analysis on microphysical property of thunderstorm with light precipitation over the Qinghai-Xizang Plateau. *Plateau Meteorology*, **30**(2), 288–298. (in Chinese with English abstract)

Dolan, B., S. A. Rutledge, S. Lim, V. Chandrasekar, and M. Thurai, 2013: A robust C-band hydrometeor identification algorithm and application to a long-term polarimetric radar dataset. *J. Appl. Meteorol. Climatol.*, **52**(9), 2162–2186, https://doi.org/10.1175/JAMC-D-12-0275.1.

Doviak, R. J., and D. S. Zrnić, 2006: *Doppler Radar and Weather Observations*. 2nd ed. Dover Publications, 562 pp.

Fujinami, H., S. Nomura, and T. Yasunari, 2005: Characteristics of diurnal variations in convection and precipitation over the Southern Tibetan Plateau during summer. *SOLA*, **1**, 49–52, https://doi.org/10.2151/sola.2005-014.

Giangrande, S. E., T. Toto, A. Bansemer, M. R. Kumjian, S. Mishra, and A. V. Ryzhkov, 2016: Insights into riming and aggregation processes as revealed by aircraft, radar, and disdrometer observations for a 27 April 2011 widespread precipitation event. *J. Geophys. Res.: Atmos.*, **121**(10), 5846–5863, https://doi.org/10.1002/2015JD024537.

Griffin, E. M., T. J. Schuur, and A. V. Ryzhkov, 2018: A polarimetric analysis of ice microphysical processes in snow, using Quasi-Vertical Profiles. *J. Appl. Meteorol. Climatol.*, **57**(1), 31–50, https://doi.org/10.1175/JAMC-D-17-0033.1.

Griffin, E. M., T. J. Schuur, A. V. Ryzhkov, H. D. Reeves, and J. C. Picca, 2014: A polarimetric and microphysical investigation of the northeast Blizzard of 8–9 February 2013. *Wea. Forecasting*, **29**, 1271–1294, https://doi.org/10.1175/WAF-D-14-00056.1.

Hersbach, H., and Coauthors. 2018: ERA5 hourly data on pressure levels from 1959 to present. Copernicus Climate Change Service (C3S) Climate Data Store (CDS), https://doi.org/10.24381/cds.bd0915c6.

Homeyer, C. R., and K. P. Bowman, 2017: Algorithm description document for version 3.1 of the three-dimensional gridded NEXRAD WSR-88D radar (GridRad) dataset. University of Oklahoma–Texas A&M University Tech. Rep., 23 pp. [Available online from http: //gridrad. org/pdf/GridRad-v3. 1-Algorithm-Description. pdf]

Jameson, A. R., 1992: The effect of temperature on attenuation-correction schemes in rain using polarization propagation differential phase shift. *J. Appl. Meteorol.*, **31**(9), 1106–1118, https://doi.org/10.1175/1520-0450(1992)031<1106:TEOTOA>2.0.CO;2.

Jensen, M. P., and Coauthors, 2016: The midlatitude continental convective clouds experiment (MC3E). *Bull. Amer. Meteor. Soc.*, **97**(9), 1667–1686, https://doi.org/10.1175/BAMS-D-14-00228.1.

Kennedy, P. C., and S. A. Rutledge, 2011: S-band dual-polarization radar observations of winter storms. *J. Appl. Meteorol. Climatol.*, **50**(4), 844–858, https://doi.org/10.1175/2010JAMC2558.1.

Kumjian, M. R., and K. A. Lombardo, 2017: Insights into the evolving microphysical and kinematic structure of northeastern U. S. winter storms from dual-polarization Doppler radar. *Mon. Wea. Rev.*, **145**(3), 1033–1061, https://doi.org/10.1175/MWR-D-15-0451.1.

Kumjian, M. R., S. A. Rutledge, R. M. Rasmussen, P. C. Kennedy, and M. Dixon, 2014: High-resolution polarimetric radar observations of snow-generating cells. *J. Appl. Meteorol. Climatol.*, **53**, 1636–1658, https://doi.org/10.1175/JAMC-D-13-0312.1.

Li, D. L., G. L. Ji, and L. Z. Lü, 2001: Impact of Tibetan Plateau surface heating field intensity on Northern Hemispherical general circulations and weather and the climate of China. *Sci. China Ser. D: Earth Sci.*, **44**(S1), 390–399, https://doi.org/10.1007/BF02912011.

Moisseev, D. N., S. Lautaportti, J. Tyynela, and S. Lim, 2015: Dual-polarization radar signatures in snowstorms: Role of snowflake aggregation. *J. Geophys. Res.: Atmos.*, **120**(24), 12 644–12 655, https://doi.org/10.1002/2015JD023884.

Pang, Z. H., D. H. Wang, X. L. Jiang, and M. H. Zhang, 2019: Analysis on thermodynamic characteristics of summer convective precipitation in the Qinghai-Tibet Plateau experimental region based on constrained objective variational analysis. *Chinese Journal of Atmospheric Sciences*, **43**(3), 511–524, https://doi.org/10.3878/j.issn.1006-9895.1806.18135. (in Chinese with English abstract)

Park, S. G., V. N. Bringi, V. Chandrasekar, M. Maki, and K. Iwanami, 2005: Correction of radar reflectivity and differential reflectivity for rain attenuation at X band. Part I: Theoretical and empirical basis. *J. Atmos. Oceanic Technol.*, **22**(11), 1621–1632, https://doi.org/10.1175/JTECH1803.1.

Picca, J. C., D. M. Schultz, B. A. Colle, S. Ganetis, D. R. Novak, and M. J. Sienkiewicz, 2014: The value of dual-polarization radar in diagnosing the complex microphysical evolution of an intense snowband. *Bull. Amer. Meteor. Soc.*, **95**(12), 1825–1834, https://doi.org/10.1175/BAMS-D-13-00258.1.

Ruan, Y., Z. Ruan, M. Wei, R. Ge, F. Li Feng, and L. Jin, 2018: Research of the vertical structure of summer convective precipitation cloud over the Qinghai-Tibetan Plateau by C-FMCW Radar. *Plateau Meteorology*, **37**(1), 93–105, https://doi.org/10.7522/j.issn.1000-0534.2017.00025. (in Chinese with English abstract)

Ryzhkov, A., P. F. Zhang, H. Reeves, M. Kumjian, T. Tschallener, S. Trömel, and C. Simmer, 2016: Quasi-vertical profiles—A new way to look at polarimetric radar data. *J. Atmos. Oceanic Technol.*, **33**(3), 551–562, https://doi.org/10.

1175/JTECH-D-15-0020.1.

Ryzhkov, A. V., and D. S. Zrnić, 1998: Discrimination between rain and snow with a polarimetric radar. *J. Appl. Meteorol.*, **37**, 1228–1240, https://doi.org/10.1175/1520-0450(1998)037<1228:DBRASW>2.0.CO;2.

Ryzhkov, A. V., and D. S. Zrnić, 2019: Polarimetric microphysical retrievals. *Radar Polarimetry for Weather Observations*, A. V. Ryzhkov and D. S. Zrnic, Eds., Springer, 435–464, https://doi.org/10.1007/978-3-030-05093-1_11.

Ryzhkov, A. V., D. S. Zrnić, and B. A. Gordon, 1998: Polarimetric method for ice water content determination. *J. Appl. Meteorol.*, **37**, 125–134, https://doi.org/10.1175/1520-0450(1998)037,0125:PMFIWC.2.0.CO;2.

Ryzhkov, A. V., P. Bukovcic, A. Murphy, P. F. Zhang, and G. McFarquhar, 2018: Ice microphysical retrievals using polarimetric radar data. *10th European Conference on Radar in Meteorology and Hydrology*, The Netherlands. Retrieved from https://projects.knmi.nl/erad2018/ERAD2018_extended_abstract_040.pdf.

Schneebeli, M., N. Dawes, M. Lehning, and A. Berne, 2013: High-resolution vertical profiles of X-band polarimetric radar observables during snowfall in the Swiss Alps. *J. Appl. Meteorol. Climatol.*, **52**(2), 378–394, https://doi.org/10.1175/JAMC-D-12-015.1.

Schrom, R. S., M. R. Kumjian, and Y. H. Lu, 2015: Polarimetric radar signatures of dendritic growth zones within Colorado winter storms. *J. Appl. Meteorol. Climatol.*, **54**(12), 2365–2388, https://doi.org/10.1175/JAMC-D-15-0004.1.

Shusse, Y., K. Nakagawa, N. Takahashi, S. Satoh, and T. Iguchi, 2009: Characteristics of polarimetric radar variables in three types of rainfalls in a Baiu front event over the East China Sea. *J. Meteor. Soc. Japan*, **87**(5), 865–875, https://doi.org/10.2151/jmsj.87.865.

Snyder, J. C., H. B. Bluestein, G. F. Zhang, and S. J. Frasier, 2010: Attenuation correction and hydrometeor classification of high-resolution, X-band, dual-polarized mobile radar measurements in severe convective storms. *J. Atmos. Oceanic Technol.*, **27**(12), 1979–2001, https://doi.org/10.1175/2010JTECHA1356.1.

Sulia, K. J., and J. Y. Harrington, 2011: Ice aspect ratio influences on mixed-phase clouds: Impacts on phase partitioning in parcel models. *J. Geophys. Res.: Atmos.*, **116**, D21309, https://doi.org/10.1029/2011JD016298.

Tang, J., X. L. Guo, and Y. Chang, 2018: Numerical studies on microphysical properties of clouds and precipitation in the summer of 2014 over the Tibetan Plateau. *Acta Meteorologica Sinica*, **76**(6), 1053–1068, https://doi.org/10.11676/qxxb2018.054. (in Chinese with English abstract)

Trömel, S., A. V. Ryzhkov, B. Hickman, K. Mühlbauer, and C. Simmer, 2019: Polarimetric radar variables in the layers of melting and dendritic growth at X band-implications for a nowcasting strategy in stratiform rain. *J. Appl. Meteorol. Climatol.*, **58**, 2497–2522, https://doi.org/10.1175/JAMC-D-19-0056.1.

Wang, H., and X. L. Guo, 2018: Comparative analyses of vertical structure of a deep convective cloud with multi-source satellite and ground-based radar observational data at Naqu over the Tibetan Plateau. *Acta Meteorologica Sinica*, **76**(6), 996–1013, https://doi.org/10.11676/qxxb2018.049. (in Chinese with English abstract)

Wang, H., H. C. Lei, and J. F. Yang, 2017: Microphysical processes of a stratiform precipitation event over eastern China: Analysis using micro rain radar data. *Adv. Atmos. Sci.*, **34**(12), 1472–1482, https://doi.org/10.1007/s00376-017-7005-6.

Wang, H., H. C. Lei, Deligeri, L. G. Li, W. A. Xiao, Y. C. Hong, and M. Y. Huang, 2002: A numerical simulation of characteristics of convective cloud at the upper reaches of the Yellow River. *Climatic and Environmental Research*, **7**(4), 397–408, https://doi.org/10.3878/j.issn.1006-9585.2002.04.03. (in Chinese with English abstract)

Wang, Y. T., and V. Chandrasekar, 2010: Quantitative precipitation estimation in the CASA X-band dual-polarization radar network. *J. Atmos. Oceanic Technol.*, **27**(10), 1665–1676, https://doi.org/10.1175/2010JTECHA1419.1.

Williams, E. R., and Coauthors, 2015: Measurements of differential reflectivity in snowstorms and warm season stratiform systems. *J. Appl. Meteorol. Climatol.*, **54**(3), 573–595, https://doi.org/10.1175/JAMC-D-14-0020.1.

Wu, G. X., and Y. S. Zhang, 1998: Tibetan Plateau forcing and the timing of the monsoon onset over South Asia and the South China Sea. *Mon. Wea. Rev.*, **126**(4), 913–927, https://doi.org/10.1175/1520-0493(1998)126<0913:TPFATT>2.0.CO;2.

Xu, X. D., C. G. Lu, X. H. Shi, and Y. H. Ding, 2010: Large-scale topography of China: A factor for the seasonal progression of the Meiyu rainband? *J. Geophys. Res.: Atmos.*, **115**, D02110, https://doi.org/10.1029/2009JD012444.

Xu, X. D., T. L. Zhao, C. G. Lu, and X. H. Shi, 2014: Characteristics of the water cycle in the atmosphere over the Tibetan Plateau. *Acta Meteorologica Sinica*, **72**(6), 1079–1095, https://doi.org/10.11676/qxxb2014.091. (in Chinese with English abstract)

Xu, X. D., L. L. Dong, Y. Zhao, and Y. J. Wang, 2019: Effect of the Asian Water Tower over the Qinghai-Tibet Plateau and the characteristics of atmospheric water circulation. *Chinese Science Bulletin*, **64**(27), 2830–2841, https://doi.org/10.1360/TB-2019-0203. (in Chinese with English abstract)

Yeh, T. C., and C. C. Chang, 1974: Preliminary experimental simulation on heating effect of Tibetan Plateau on general circulation over eastern Asia in summer. *Scientia Sinica*, **17**(3), 397–420.

Yue, Z. G., X. Yu, G. H. Liu, J. Dai, Y. N. Zhu, X. H. Xu, Y. Hui, and C. Chen, 2018: NPP/VIIRS satellite retrieval of summer convective cloud microphysical properties over the Tibetan Plateau. *Acta Meteorologica Sinica*, **76**(6), 968–982, https://doi.org/10.11676/qxxb2018.051. (in Chinese with English abstract)

Zhang, T., J. F. Zheng, and Y. X. Liu, 2019: A study on the vertical structure and microphysical characteristic of convective cloud and precipitation over Tibetan Plateau by using Ka-band cloud radar. *Journal of Infrared and Millimeter Waves*, **38**(6), 777–789, https://doi.org/10.11972/j.issn.1001-9014.2019.06.015. (in Chinese with English abstract)

Zhang, Y. X., J. B. Tian, P. L. Zhang, L. M. Xue, and X. Y. Kang, 2021: Analysis of circulation situation and operating conditions for artificial precipitation enhancement in Qinghai in 2018. *Journal of the Meteorological Sciences*, **41**(5), 703–710, https://doi.org/10.12306/2021jms.0022. (in Chinese with English abstract)

Zhao, P., and Coauthors, 2018: The Tibetan Plateau surface-atmosphere coupling system and its weather and climate effects: The Third Tibetan Plateau Atmospheric Scientific Experiment. *Acta Meteorologica Sinica*, **76**(6), 833–860, https://doi.org/10.11676/qxxb2018.060. (in Chinese with English abstract)